Supplementary Information for:

Optomechanical sensor network with fiber Bragg gratings

Shiwei Yang[1*], Qiang Zhang[1,2*†], Linrun Yang[1*], Hanghua Liu[1], Quansen Wang[1], Pengfei Zhang[1,2], Heng Shen[1,2‡], Yongmin Li[1,2§]

[1]State Key Laboratory of Quantum Optics and Quantum Optics Devices, Institute of Opto-Electronics, Shanxi University, Taiyuan 030006, China

[2]Collaborative Innovation Center of Extreme Optics, Shanxi University, Taiyuan 030006, China

CONTENTS

S1. Principle of phase-shifted fiber Bragg grating (PFBG)

S2. Mechanical resonator

S2.1 Fiber mechanical resonator

S2.2 Terfenol-D mechanical resonator

S3. Optomechanical coupling between PFBG and Terfenol-D MR

S4. Noise from thermal Brownian motion

S5. Experimental results

S5.1 Performances of multiple FOMMs

S5.2 Linear response range of the FOMM for AC magnetic fields

S5.3 Responses of the sensor network to DC magnetic fields

Supplementary References

*These authors contributed equally to this work.

† qzhang@sxu.edu.cn

‡ hengshen@nbi.dk

§ yongmin@sxu.edu.cn

S1. Principle of phase-shifted fiber Bragg grating (PFBG)

A phase-shifted fiber Bragg grating could be formed by introducing a phase shift in a standard fiber Bragg grating, and a sharp resonant dip will arise within the reflective spectrum of the fiber Bragg grating. The sharp resonant dip has a narrower bandwidth and is used as optical filters extensively. Fig. 1(a) illustrates a schematic diagram of a typical fiber Bragg grating (FBG), including the variation of the core refractive index. The refractive index within the grating region varies uniformly and sinusoidally along the fiber axis according to the following equation:

$$n_1(z)=\begin{cases} n_1+\Delta n_1(z) & 0<z<L \\ n_1 & z<0\,\&\,z>L \end{cases} \tag{S1}$$

$$\Delta n_1(z)=\Delta n\sin\left(\frac{2\pi}{\Lambda}z\right) \tag{S2}$$

where L is the length of the grating region, n_1 is the initial refractive index of the core, $\Delta n_1(z)$ represents the axial refractive index distribution function in the fiber grating region, Δn is the refractive index modulation amplitude, and Λ is the period of the grating.

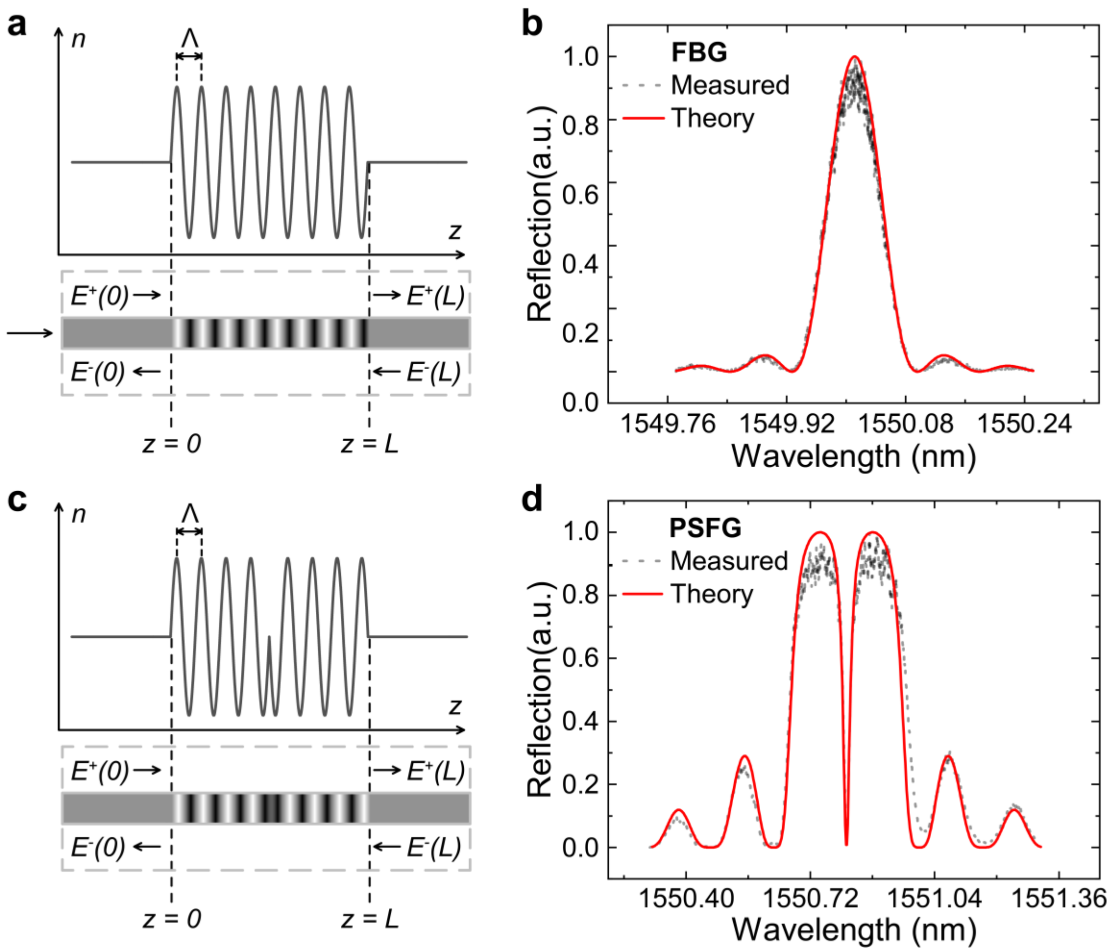

Fig. S1 **a** and **c** Core refractive indexes for typical FBG and PFBG, **b** and **d** Reflective spectra for typical FBG and PFBG.

The calculation of the reflection spectrum of the FBG can be performed using the transfer matrix method (TMM). As illustrated in the Fig 1(a), the left boundary (z = 0) of the grating is defined as the light input port and the right boundary ($z = L$) as the light output port. The forward-going mode and backward-going mode are defined as E^+ and E^-, respectively. The relationship between different modes can be mathematically represented through the matrix equation [1,2]:

$$\begin{bmatrix} E^+(L) \\ E^-(L) \end{bmatrix} = F_L \begin{bmatrix} E^+(0) \\ E^-(0) \end{bmatrix} = \begin{bmatrix} m & n \\ n^* & m^* \end{bmatrix} \begin{bmatrix} E^+(0) \\ E^-(0) \end{bmatrix} \tag{S3}$$

$$\begin{aligned} m &= \cosh(\gamma L) - i\frac{\sigma}{\gamma}\sinh(\gamma L) \\ n &= -i\frac{\kappa}{\gamma}\sinh(\gamma L) \end{aligned} \tag{S4}$$

where $\sigma = 2\pi n_{\mathrm{eff}}(1/\lambda - 1/\lambda_B)$, $\lambda_B = 2n_{\mathrm{eff}}\Lambda$ is the Bragg wavelength and n_{eff} is the effective refractive index of the grating. F_L is the fundamental transmission matrix characterizing the FBG of length L. The coupling coefficient $\kappa = \pi\delta n_{\mathrm{eff}}/\lambda$ quantifies the interaction between the forward-going mode and the backward-going mode, where δn_{eff} stands for the effective refractive index modulation value. The parameter $\gamma = (\kappa^2 - \sigma^2)^{1/2}$.

By applying the boundary condition $E^-(L) = 0$, the reflection and transmission spectra of the FBG are given by:

$$\begin{aligned} R &= \left|\frac{E^-(0)}{E^+(0)}\right|^2 = \left|-\frac{n^*}{m^*}\right|^2 \\ T &= \left|\frac{E^+(L)}{E^+(0)}\right|^2 = \left|m - \frac{n \cdot n^*}{m^*}\right|^2 \end{aligned} \tag{S5}$$

To compare the theory to an experimental measurement, Fig. 1(b) shows the calculated (red solid line, λ_B = 1550.011 nm, n_{eff} = 1.46, $\delta n_{\mathrm{eff}} = 2\times10^{-5}$, L = 9.8 mm) and measured (gray dotted line) normalized reflection spectrum of a commercial FBG.

Fig. 1(c) illustrates a schematic diagram of a typical phase-shifted fiber Bragg grating (PFBG). Its refractive index variation within the uniform regions is consistent with that of the FBG, exhibiting a uniform sine wave distribution. However, the phase changes abruptly at point $z = L/2$, with a phase shift of $\varphi = \pi$.

The piecewise-continuous axial refractive index modulation profile of the PFBG necessitates representation through a piecewise function:

$$\Delta n_1(z) = \begin{cases} \Delta n \cos\left(\dfrac{2\pi}{\Lambda} z\right) & 0 < z < L/2 \\ \Delta n \cos\left(\dfrac{2\pi}{\Lambda} z + \varphi\right) & L/2 < z < L \end{cases} \tag{S6}$$

This characteristic of the PFBG is represented in the transmission matrix by inserting a phase-shift matrix F_φ between two basic transmission matrices:

$$\begin{bmatrix} E^+(L) \\ E^-(L) \end{bmatrix} = F_{L/2}F_\varphi F_{L/2} \begin{bmatrix} E^+(0) \\ E^-(0) \end{bmatrix} = \begin{bmatrix} p & q \\ q^* & p^* \end{bmatrix} \begin{bmatrix} e^{-i\varphi/2} & 0 \\ 0 & e^{i\varphi/2} \end{bmatrix} \begin{bmatrix} p & q \\ q^* & p^* \end{bmatrix} \begin{bmatrix} E^+(0) \\ E^-(0) \end{bmatrix} \tag{S7}$$

$$p = \cosh\left(\gamma\frac{L}{2}\right) - i\frac{\sigma}{\gamma}\sinh\left(\gamma\frac{L}{2}\right)$$
$$q = -i\frac{\kappa}{\gamma}\sinh\left(\gamma\frac{L}{2}\right) \tag{S8}$$

By applying the boundary condition $E^{-}(L) = 0$, the PFBG's reflection and transmission spectra are given by:

$$R = \left|\frac{E^{-}(0)}{E^{+}(0)}\right|^2 = \left|-\frac{\left(p + e^{2i\varphi}p^{*}\right)q^{*}}{e^{2i\varphi}p^{*2} + qq^{*}}\right|^2$$
$$T = \left|\frac{E^{+}(L)}{E^{+}(0)}\right|^2 = \left|\frac{e^{i\varphi}\left(pp^{*} - qq^{*}\right)^2}{e^{2i\varphi}p^{*2} + qq^{*}}\right|^2 \tag{S9}$$

Similarly, Fig. 1(d) shows the calculated (red line, λ_B = 1550.81 nm, n_{eff} = 1.46, $\delta n_{eff} = 14\times10^{-5}$, L = 9.6 mm) and measured (gray dotted line) normalized reflection spectrum of a commercial PFBG. Fig. S2 presents the measured reflective spectra of six PFBGs, and the bandwidths are 51.5 pm, 15.3 pm, 15.6 pm, 37.1 pm, 36.6 pm, and 1.4 pm, respectively.

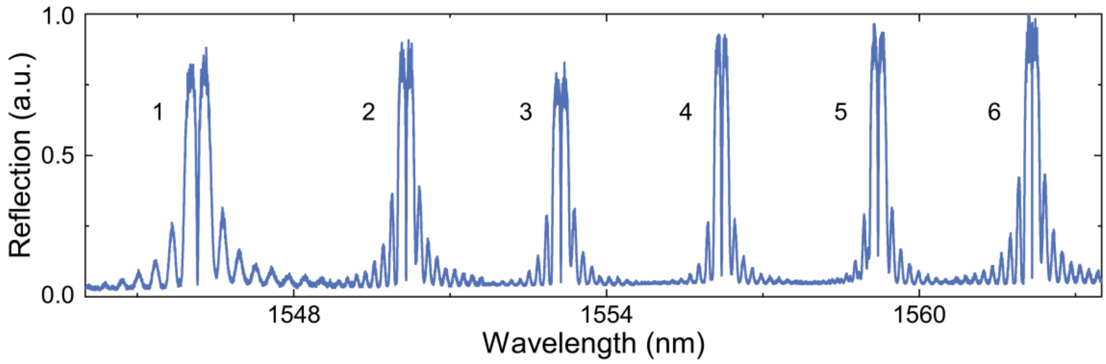

Fig. S2 Reflective spectra of six PFBGs in our experiments.

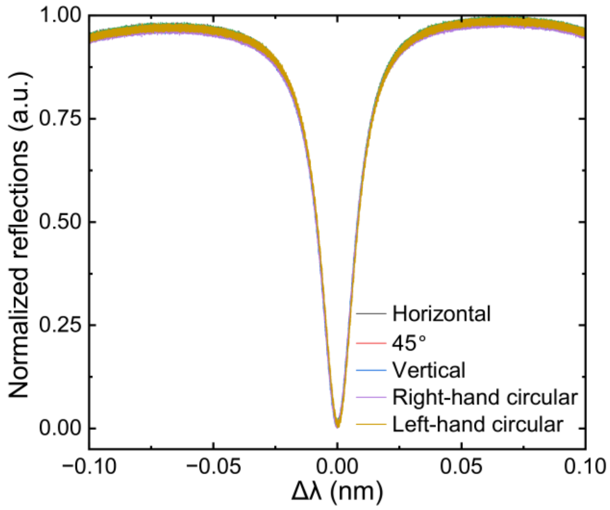

Fig. S3 Normalized reflections of a PFBG as a function of lights with different polarizations (horizontal, 45°, vertical, right-hand circular, and left-hand circular).

We also test the response of a PFBG to lights with different polarizations by varying the polarization of incident lights. Fig. S3 shows that the responses are uniform for different polarizations.

S2. Mechanical resonator

The mechanical resonator model is described in Fig. S4. The mechanical resonator with mass m displaces x when subjected to an external force F, and the motion equation is given by

$$m\ddot{x}+m\gamma\dot{x}+m\omega_m^2 x=F \quad , \tag{S10}$$

where ω_m and $\gamma=\omega_m/Q_m$ are the mechanical resonant frequency and decay rate of the mechanical resonator, and Q_m is quality factor. The displacement in Fourier space is

$$x(\omega)=\chi(\omega)\frac{F(\omega)}{m}=\frac{1}{\omega_m^2-\omega^2+i\,\omega\omega_m/Q_m}\frac{F(\omega)}{m} \; . \tag{S11}$$

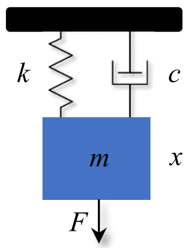

Fig. S4 Schematic diagram of a typical mechanical resonator.

S2.1 Fiber mechanical resonator

In this work, the FOMM is fabricated by inserting a commercial standard PFBG into two silica capillaries and filling the gap with UV glue as shown in Fig. S5. A clamped-clamped fiber mechanical resonator is formed.

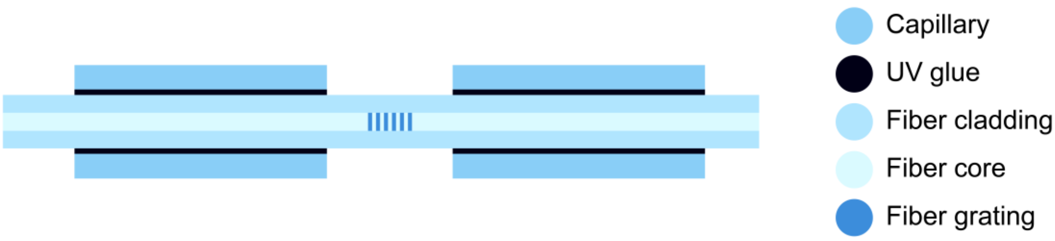

Fig. S5 Structure of the FOMM

For the fiber mechanical resonator with a 10.5 mm SMF in Fig. 3, the mode shapes of flexural modes are shown in Fig. S6a. The resonant frequencies and quality factors of the flexural modes are dependent on the stress in the fiber mechanical resonator [51]. As shown in Fig. 3, the resonant frequency (quality factor) of the fundamental mode of the fiber mechanical resonator are 7.82 kHz (150), 8.14 kHz (220), and 8.89 kHz (290) when the magnetic field are 0 Gs, 20 Gs, and 50 Gs. Fig. S6b shows power spectral densities (PSD) of the fundamental and third modes for a fiber MR with a length of 8 mm and a diameter of 125μm.

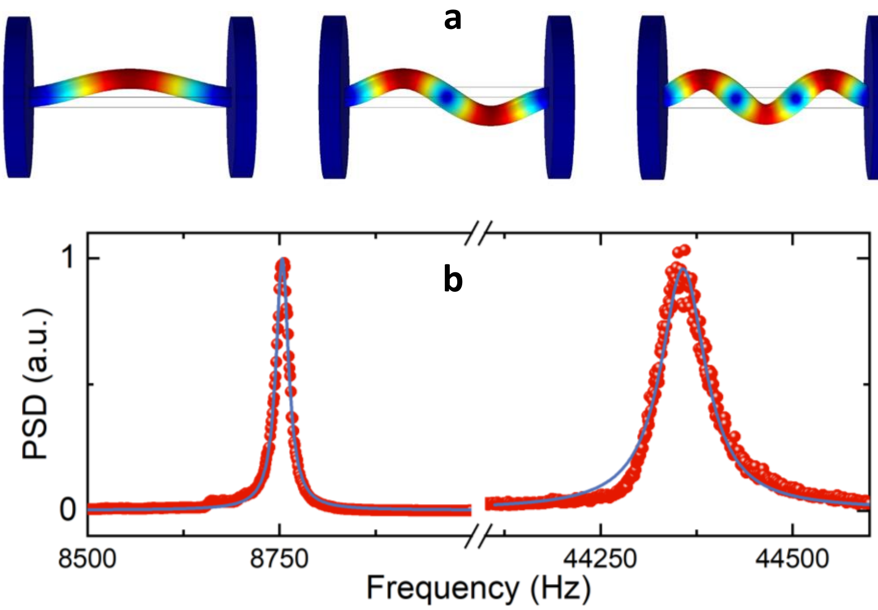

Fig. S6 **a** Mode shapes of the first three flexural modes of the fiber MR, **b** Power spectral densities (PSD) of a fiber MR with a length of 8 mm and a diameter of 125μm.

S2.2 Terfenol-D mechanical resonator

In this work, the Terfenol-D MR is a cuboid, where the stretching modes of the Terfenol-D MR have bigger optomechanical coupling constant because the deformation of the stretching modes is coaxial with the PFBG. Fig. S7 shows the mode shapes of the first three stretching modes of the Terfenol-D MR.

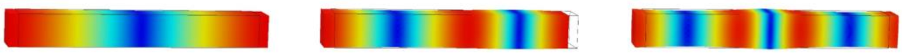

Fig. S7 Mode shapes of the first three stretching modes of the Terfenol-D MR

Terfenol-D MR enables the detection of magnetic fields, and further brings some tunability of detection range. As stated in the manuscript and displayed in Fig. 3, the resonant frequency and *Q*-factor of the Terfenol-D mechanical resonator both decrease when a bias DC magnetic field is applied to the Terfenol-D mechanical resonator. This has been observed by Kellogg and A. Flatau, and the associated results were shown in Fig. 15 of the paper [R. Kellogg and A. Flatau, Wide Band Tunable Mechanical Resonator Employing the ΔE Effect of Terfenol-D, Journal of Intelligent Material Systems and Structures 15, 355 (2004), cited as Ref. 54].

Regarding the variation of the resonance frequency, one can look at the equation determined the resonance frequency of the *n*-th stretching mode of the Terfenol-D mechanical resonator $f_n=n(E/\rho)^{1/2}/2l$. Here, E is Young's modulus, l is the length, and ρ is density. The resonant frequency is proportional to the E and inversely proportional to the length l. As a bias DC magnetic field is applied, the resonant frequency decreases due to the reduction of the E and the increase of the l.

On the other hand, regarding the performance degradation, the authors have discussed in Ref. 54, "Evidenced by acceleration transmissibility decreases from 14.3 at H = 0 to approximately 7.5 at H = 60.7kA/m, as the modulus decreases with increasing H, the damping also increases". To understand this coupling between magnetism and vibrations, one needs to explain the underlying physics in terms of magnetic material physics. We find the associated discussion in the paper [K. B. Hathaway, A. E. Clark, and J. P. Teter, Magnetomechanical Damping in Giant Magnetostriction Alloys, Metallurgical and Materials Transactions A 26A, 2797 (1995), cited as Ref. 55]. The authors stated that, “Magnetic materials usually contain domains of different magnetization directions along the magnetically easy directions specified by the magnetocrystalline anisotropy. This reduces the overall sample energy by reducing or eliminating magnetic poles at the boundaries but at the cost of magnetocrystalline anisotropy energy within the domain walls, where M is rotated away from the easy axes. Application of a magnetic field H produces motion of these domain walls such that domains with M aligned nearest to the di-rection of H grow. Motion of domain walls can be impeded by various structural defects, producing losses when the domain walls break free of the pinning sites”.

S3. Optomechanical coupling between PFBG and Terfenol-D MR

The resonant wavelength λ_0 of a fiber Bragg grating depending on the grating period Λ is given by

$$\lambda_0 = 2n_{fiber}\Lambda \,. \tag{S12}$$

Thus, the corresponding resonant optical frequency is

$$f_{opt} = \frac{c}{2n_{fiber}^2\Lambda} \,, \tag{S13}$$

where c is the speed of light. When the Terfenol-D MR generates a deformation Δx, the grating period changes with $\Delta\Lambda = \Lambda\Delta x / L_{\mathrm{fiber}}$. Then, the optomechanical coupling constant is given by

$$g_{OM} = \frac{\Delta f_{opt}}{\Delta x} = \frac{c}{n\lambda_0 L_{fiber}} \,. \tag{S14}$$

For the sensor in Fig. 2, $n = 1.4682$, $\lambda_0 = 1550$ nm, and $L_{\mathrm{fiber}} = 2$ mm, and therefore $g_{\mathrm{OM}} = 66$ MHz/nm.

S4. Noise from thermal Brownian motion

At room temperature, the noise-equivalent acceleration (NEA) of a mechanical resonator in contact with a heat-bath is

$$a_{th} = \sqrt{\frac{4k_B T\omega_m}{mQ_m}} , \tag{S15}$$

where k_B is Boltzmann constant, T is the temperature in Kelvin. The corresponding displacement noise is [28]

$$S_{xx}^{th}(\omega) = \frac{4k_B T\omega_m}{mQ_m} \frac{1}{\left(\omega_m^2 - \omega^2\right)^2 + \left(\omega\omega_m / Q_m\right)^2} , \tag{S16}$$

and the noise power-spectral density of the probe light reflected from the PFBG is

$$S_{pp}^{th}(\omega) = \left|\frac{dP_r}{d\Delta}\right|^2 \eta_{in}^2 P_{in}^2 g_{OM}^2 S_{xx}^{th}(\omega) . \tag{S17}$$

Thus, the noise power-spectral density at ESA is given by

$$S_{ESA}^{th} = S_{pp}^{th}(\omega) G_{PD}^2 / 50 \tag{S18}$$

For the device in Fig. 2, the noise power-spectral density of the Terfenol-D MR could be achieved according to the Equation S18, where G_{PD} = 100000, is the gain of the PD, η_{in} = 0.3, P_{in} = 0.113 mW, g_{OM} = 66 MHz/nm, and $dP_r/d\Delta = 2.3 \times 10^{-8}$ Hz^{-1}, is the slope of the reflective spectrum of the PFBG.

S5. Experimental results

S5.1 Performances of multiple FOMMs

We evaluate the performances of multiple FOMMs and calibrate their DC and AC magnetic-field sensitivities as summarized in Table S1.

Table S1. Performances of the six FOMMs. D_{TR}, deformation transferring radio; FWHM, full width at half maximum of PFBGs; R_{max} is the maximum reflectivity of the PFBG; R_{min} is the reflectivity of the PFBG at phase-shift point. B_{DC}, DC magnetic-field sensitivity; B_{min}, AC magnetic-field sensitivity.

Sensors	D_{TR}	FWHM (pm)	R_{max}	R_{min}	B_{DC} (pm/Gs)	B_{min} (pT/Hz$^{1/2}$)
1	1	15.3	0.818	0.058	0.65	10.31
2	5.1	1.4	0.901	0.064	3.31	0.537
3	8.3	15.6	0.720	0.050	5.33	1.77
4	9.4	37.1	0.876	0.145	6.07	1.73
5	9.3	51.5	0.782	0.047	6.02	3.47
6	13.5	36.6	0.862	0.072	8.73	1.48

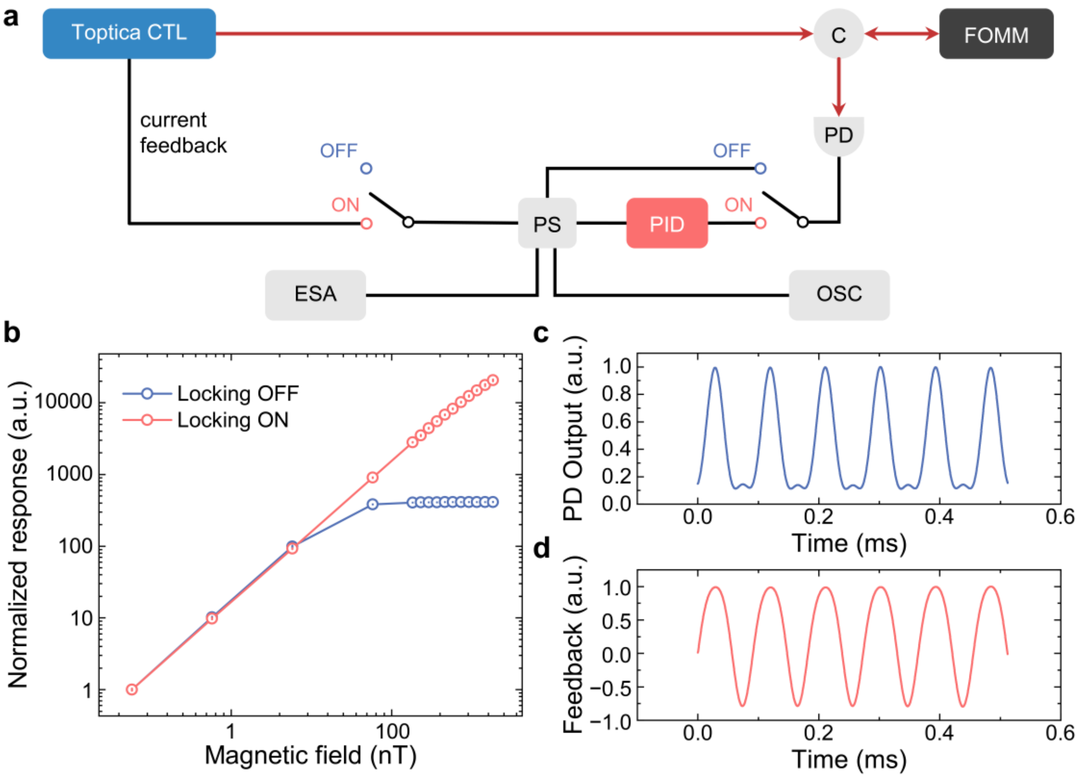

Fig. S8 Linear response ranges of the FOMM with and without locking loop. **a**, experimental setup. **b**, normalized responses of the FOMM as a function of magnetic-field strength. **c**, time response of the FOMM without locking loop. **d**, time response of the FOMM with locking loop. ESA, electrical spectrum analyzer; C, circulator; PDs, photodetectors; OSC, oscilloscope; PS, power splitter.

S5.2 Linear response range of the FOMM for AC magnetic fields

The response range of the FOMM is evaluated by varying the amplitude of the applied AC magnetic field. Fig. S8 shows the normalized response of the FOMM at the resonant frequency as a function of magnetic-field strength with (red) and without locking loop (blue). A larger linear measurement range is observed when the laser is locked to the PFBG.

Concretely, the tunable laser is locked to the PFBG using a Red Pitaya board (STEM lab 125-14) by current feedback, which has a feedback bandwidth of 100MHz. As shown in Fig. S8a, the signal from the PD is monitored by an electrical spectrum analyzer (ESA) and oscilloscope (OSC), when the feedback locking is not in service. When the feedback loop is on, the signal from the PD is transferred to a PID system for the feedback signal, which is applied to the laser by current feedback and is also monitored by the ESA and OSC. Fig. S8b presents the normalized responses of the FOMM as a function of magnetic-field strength with (red) and without (blue) locking loop. When the magnetic-field strength exceeds the linear response range of the FOMM without locking loop, the response becomes saturated, but the response with locking loop is still linear. The typical time-domain responses are shown in Fig. S8c (without locking loop) and Fig. S8d (with locking loop). With same magnetic field excitation, the response of the FOMM without locking loop is out of the linear range, but it with locking loop is not. Therefore, the linear measurement range can be indeed extended by locking the probe laser to the PFBG.

S5.3 Response of the sensor network to DC magnetic fields

We evaluate the performances of the optomechanical sensor network with nine FOMMs for DC magnetic fields as shown in Fig. S9. When the coil with a constant 52 Gs DC magnetic field moves from right to left, the response of the optomechanical sensor network is presented in Fig. S9b.

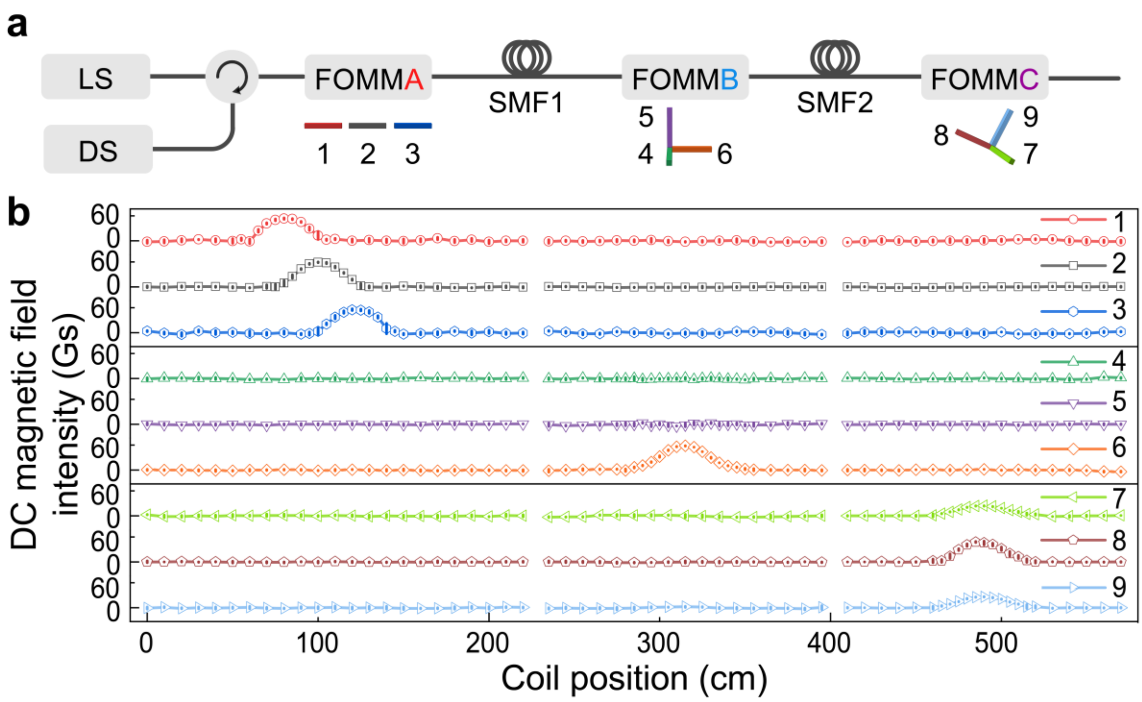

Fig. S9 Responses of the optomechanical sensor network for DC magnetic fields. **a**, Schematic diagram of the optomechanical sensor network system. **b**, Responses of the sensor network with nine FOMMs. LS: light source, DS: demodulated system, SMF1 and SMF2: 1-kilometer standard SMF.

References

[1] Erdogan T. Fiber grating spectra. *J. Lightwave Technol*. **15**, 1277–1294 (1997).
[2] Wei, L., Lit, J. W. Y. Phase-shifted Bragg grating filters with symmetrical structures. *J. Lightwave Technol*. **15**, 1405–1410 (1997).